Magnetism of Ba4Ru3 O10 revealed by density functional calculations : structural trimers behaving as coupled magnetic dimers

Guillaume Radtke, A Saúl, Yannick Klein, G Rousse

Magnetism of $Ba_4Ru_3O_{10}$ revealed by density functional calculations : structural trimers behaving as coupled magnetic dimers

G. Radtke,[1,2,*] A. Saúl,[3] Y. Klein,[1] and G. Rousse[1]

[1] *IMPMC-CNRS UMR 7590, Université Pierre et Marie Curie-Paris 6, Campus Jussieu, 4 place Jussieu F-75252 Paris Cedex 05, France*

[2] *IM2NP-CNRS UMR 7334, Aix-Marseille University, Faculté des Sciences de Saint-Jérôme, F-13397 Marseille, France*

[3] *CINaM-CNRS UMR 7325, Aix-Marseille University, Campus de Luminy, 13288 Marseille cedex 9, France*

Density functional calculations have been carried out to investigate the origin of the peculiar magnetic properties of $Ba_4Ru_3O_{10}$. These calculations suggest that, under the influence of Ru-Ru covalent bonding, structural trimers behave in this compound as strong $S = 1$ antiferromagnetic dimers ordering below T_N under the influence of weaker inter-trimer couplings.

PACS numbers: 75.47.Lx, 75.25.-j, 71.27.+a

I. INTRODUCTION

In the last 20 years, ruthenium oxides have been the topic of numerous studies because they often exhibit a strong relationship between structural, orbital and spin degrees of freedom leading to unusual physical properties[1]. For example, this interplay is responsible for the spin-singlet dimerization observed in $La_4Ru_2O_{10}$[2–6] and for the spontaneous formation of spin ($S = 1$) Haldane chains in $Tl_2Ru_2O_7$[7]. Another illustration of the complexity of Ru-oxides is the $Ca_{2-x}Sr_xRuO_4$ prototype, in which one may considerably tune the transport and magnetic properties by an isovalent substitution, the size effect being the only driving force[8]. While on the Sr-rich side, unconventional superconductivity is found with the possibility of spin-triplet pairing[9], Ca_2RuO_4 shows an orbital selective Mott transition near room temperature[10] and was proposed to be used as a temperature sensor for bolometers[11].

Recently, we have shown that the antiferromagnetic (AFM) phase transition at $T_N \sim 105$ K in $Ba_4Ru_3O_{10}$ is accompanied by drastic variations of the transport properties[12]. This compound is built from Ru_3O_{12} trimers of face-shared $Ru(2)O_6$-$Ru(1)O_6$-$Ru(2)O_6$ octahedra (Fig. 1(a) and (b)). Each trimer is connected to four neighbouring trimers through corner sharing of $Ru(2)O_6$ octahedra to form corrugated layers that are then stacked together along the b axis. This arrangement leads to the formation of zig-zag chains of $Ru(2)O_6$ octahedra running along the a axis in each layer (Fig. 1(c)). While the high-temperature susceptibility was interpreted in term of paramagnetic (PM) Ru^{4+} in the low-spin ($S = 1$) configuration, low- and intermediate-temperature magnetic properties asked for more clarifications. In particular, neutron powder diffraction patterns below T_N indicate that the Néel order is of a new kind since outer Ru(2) order in an AFM lattice while inner Ru(1) do not exhibit any ordered magnetic moment.

In this paper, based on Density Functional Theory (DFT) calculations, we investigate the electronic structure of $Ba_4Ru_3O_{10}$ and identify the metal-metal covalent bonding within the trimers as a fundamental parameter influencing the magnetic behaviour of this compound. In particular, we show how structural trimers might be considered as strong AFM dimers ordering below T_N under the influence of weaker inter-trimer couplings.

II. COMPUTATIONAL DETAILS

Electronic structure and total energy calculations were performed using the WIEN2K code[13]. This code is an implementation of the full-potential linearized augmented plane-wave method based on density-functional theory. The calculations presented hereafter were performed using the generalized gradient approximation of Perdew, Burke, and Ernzerhof (GGA)[14] for exchange and correlation. Muffin-tin spheres radii were set to 2.43 a.u. for Ba, 1.91 a.u. for Ru, and 1.69 a.u. for O in all of these calculations. When included, on-site Hubbard U term was taken into account using the method proposed by Anisimov *et al.*[15] with $U_{eff} = 2.5$ eV (J = 0 eV) typically employed for Ru-4*d* states[4] and Spin-orbit coupling (SO) was treated using scalar-relativistic wavefunctions in a second-variational procedure[16]. All these calculations have been performed using the low-temperature (determined at 10 K) experimental crystal structure[12].

III. RESULTS

A. Electronic structure

$Ba_4Ru_3O_{10}$ is described in the orthorhombic *Cmca* space-group, with lattice parameters $a = 5.767$ Å, $b = 13.245$ Å and $c = 13.064$ Å and containing four formula units per cell. Ru atons are distributed among two Wyckoff sites, *4a* at (0,0,0) corresponding to the Ru(1) in the middle of the trimer and *8f* at (0,*y*,*z*) with $y \approx 0.87$ and $z \approx 0.14$ corresponding to the Ru(2) at

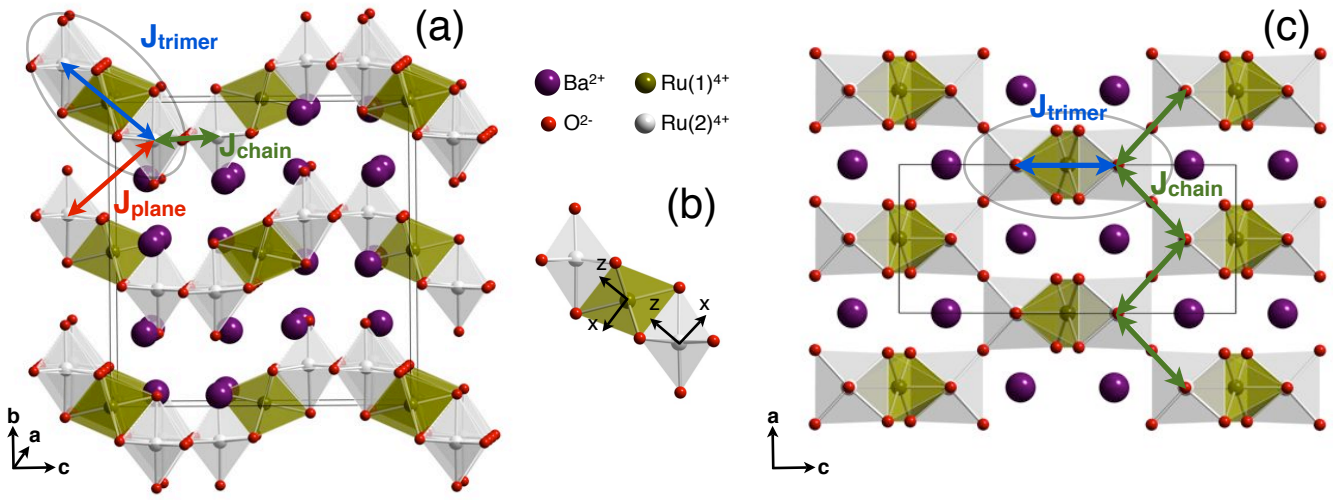

FIG. 1: (color online) (a) Atomic structure of $Ba_4Ru_3O_{10}$. (b) Local system of coordinates employed to decompose Ru-4d LDOS. (c) Structure of a corrugated layer observed along the b axis. Dominant magnetic couplings occurring between Ru(2) ions are indicated in (a) and (c) and circles highlight the structural trimers.

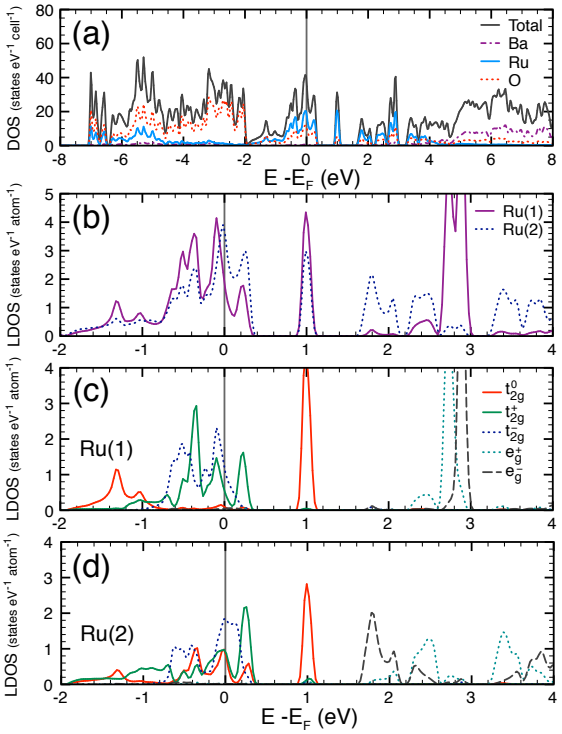

FIG. 2: (color online) (a) Non-magnetic DOS of $Ba_4Ru_3O_{10}$ calculated in GGA (b) Detail of Ru(1) and Ru(2) paramagnetic LDOS. (c) and (d) Ru(1) and Ru(2)-4d paramagnetic LDOS decomposed on the real t_{2g}^0, t_{2g}^+, t_{2g}^-, e_g^+, e_g^- orbitals and with the z axis along the metal-metal bond direction within the trimer.

the edges. The basic features of the electronic structure of $Ba_4Ru_3O_{10}$ are shown in the total and local densities of states (LDOS) obtained from a non-magnetic calculation and presented in Fig. 2(a). The valence band is essentially built from O-2p states located between -7 and -2 eV whereas Ru-4d states are found at higher energies, mainly between -2 and +4 eV. A metallic solution is found, consistent with a filling of two third of the Ru-4d t_{2g} bands for both Ru sites as expected for Ru^{4+}. A closer inspection of the Ru(1) and Ru(2) LDOS (Fig.2(b)) however, reveals a first interesting feature of this compound : the LDOS of Ru(2) at the Fermi level ($N(E_f) \approx 3.7$ eV^{-1}atom^{-1}) is almost twice as large as that of Ru(1) ($N(E_f) \approx 1.8$ eV^{-1}atom^{-1}). Although not strictly applicable to these LDOS, Stoner criterion might still appear here as a useful guide predicting a qualitatively different behaviour of these two ions towards ferromagnetic instability, as already noted by Streltsov and Khomskii[17]. One might indeed expect a weaker energy lowering through spin-polarization for Ru(1) than for Ru(2). This is precisely what a (GGA) ferromagnetic calculation reveals : a more stable solution is found through spin polarization (by about 115 meV/f.u.) but a larger magnetic moment is found on Ru(2) ions ($\sim 0.94\ \mu_B$) than on Ru(1) ions ($\sim 0.34\ \mu_B$). To understand the mechanism leading to this peculiar imbalance in the behaviour of the two inequivalent Ru ions, it is instructive to analyse the symmetry of the Ru-4d states close to the Fermi level. To account for the particular face-shared geometry of the coordination octahedra within the trimer, Ru-4d LDOS have been decomposed on a set of alternative real orbitals obtained for a quantization z axis taken along the threefold axis of the perfect octahedron. The expression of these orbitals in the basis of the conven-

TABLE I: Magnetic moments (in μ_B) in the Ru muffin-tin spheres calculated for a FM and ground-state AFM orders.

	GGA		GGA+U	
	Ru(1)	Ru(2)	Ru(1)	Ru(2)
FM	0.34	0.94	0.09	1.12
AFM	0.0	0.88	0.0	1.22

tional cubic orbitals is given by[18]

$$
\begin{aligned}
|t_{2g}^0\rangle &= |d_{z^2}\rangle \\
|t_{2g}^+\rangle &= \sqrt{\frac{2}{3}}|d_{x^2-y^2}\rangle - \sqrt{\frac{1}{3}}|d_{xz}\rangle \\
|t_{2g}^-\rangle &= \sqrt{\frac{2}{3}}|d_{xy}\rangle + \sqrt{\frac{1}{3}}|d_{yz}\rangle
\end{aligned}
$$

and

$$
\begin{aligned}
|e_g^+\rangle &= \sqrt{\frac{1}{3}}|d_{x^2-y^2}\rangle + \sqrt{\frac{2}{3}}|d_{xz}\rangle \\
|e_g^-\rangle &= \sqrt{\frac{1}{3}}|d_{xy}\rangle - \sqrt{\frac{2}{3}}|d_{yz}\rangle
\end{aligned}
$$

and the local systems of coordinates for both Ru(1) and Ru(2) sites are shown in Fig. 1(b). Although the particular structure of $Ba_4Ru_3O_{10}$ allows for local distortions of the octahedra by breaking the third order axis of the trimer (the point group symmetry of the Ru(1) and Ru(2) sites is therefore not O_h but we keep the t_{2g} and e_g notations here for convenience), this choice proves particularly useful as it brings the local z axis along the metal-metal direction. t_{2g}^0 orbitals have therefore their main lobes pointing through the face shared by $Ru(1)O_6$ and $Ru(2)O_6$ coordination octahedra, t_{2g}^+ and t_{2g}^- lobes point toward the middle of the edges shared by these octahedra whereas e_g^+ and e_g^- orbitals point directly toward the O ions. LDOS for Ru(1) and Ru(2), shown respectively in Fig. 2(c) and (d), display large crystal-field splittings between low-lying t_{2g} and high-lying e_g states. A striking feature however occurs in the t_{2g} states : whereas t_{2g}^+ and t_{2g}^- states are found around the Fermi level and exhibit a moderate energy dispersion, the t_{2g}^0 states appear for Ru(2) in three regions respectively located below, at and above the Fermi level separated from each other by about 1 eV. The t_{2g}^0 LDOS for Ru(1) echoes that of Ru(2) with however the absence of states at the Fermi level. This pattern is directly related to the large σ bonding covalent interaction experienced by these orbitals. Molecular orbitals arising within the trimer can be pictured using a simple three-site model accounting for hopping $t < 0$ and overlap $S > 0$ integrals (the Ru-Ru distance of ~ 2.55 Å here is much shorter than in metallic Ru) between nearest-neighbours. Three bonding, non-bonding and anti-bonding molecular orbitals are formed, of respective energies $\epsilon_b = \sqrt{2}t/(1+\sqrt{2}S)$, $\epsilon_{nb} = 0$ and $\epsilon_{ab} = -\sqrt{2}t/(1-\sqrt{2}S)$. The expression of these molecular orbitals in term of Ru-t_{2g}^0 states for a trimer $|\phi'_{(2)}\rangle$, $|\phi_{(1)}\rangle$ and $|\phi''_{(2)}\rangle$ are respectively :

$$
\begin{aligned}
|\psi_b\rangle &= \frac{1}{\sqrt{4\left(1+\sqrt{2}S\right)}}\left(|\phi'_{(2)}\rangle + \sqrt{2}|\phi_{(1)}\rangle + |\phi''_{(2)}\rangle\right) \\
|\psi_{nb}\rangle &= \frac{1}{\sqrt{2}}\left(|\phi'_{(2)}\rangle - |\phi''_{(2)}\rangle\right) \\
|\psi_{ab}\rangle &= \frac{1}{\sqrt{4\left(1-\sqrt{2}S\right)}}\left(|\phi'_{(2)}\rangle - \sqrt{2}|\phi_1\rangle + |\phi''_{(2)}\rangle\right)
\end{aligned}
$$

The non-bonding molecular orbital is therefore built from Ru(2)-t_{2g}^0 states only and explains, at least partially, the reduced density of states at the Fermi level observed for Ru(1) as seen in Fig.2(b). These results are consistent with the work published recently by Streltsov and Khomskii[17].

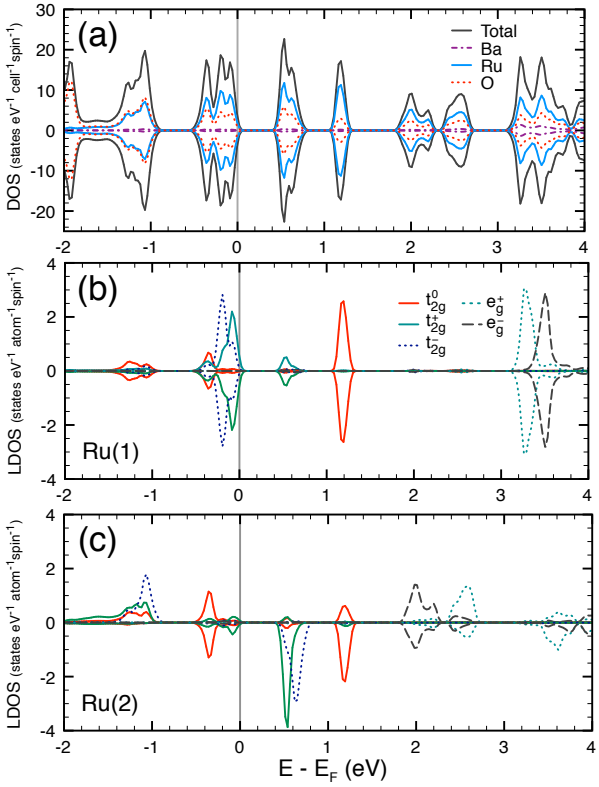

FIG. 3: (color online) (a) DOS in $Ba_4Ru_3O_{10}$ calculated in GGA+U for the ground-state AFM order. (b) Corresponding 4d-LDOS of Ru(1) and (c) of one the Ru(2) of a trimer.

B. Magnetic order and couplings

To determine the ground-state magnetic order of this compound, the total energies of 30 distinct spin configurations compatible with a single orthorhombic conventional cell of $Ba_4Ru_3O_{10}$ have been computed in GGA and GGA+U. In both cases, the ground-state configuration is the same and corresponds to an AFM arrangement

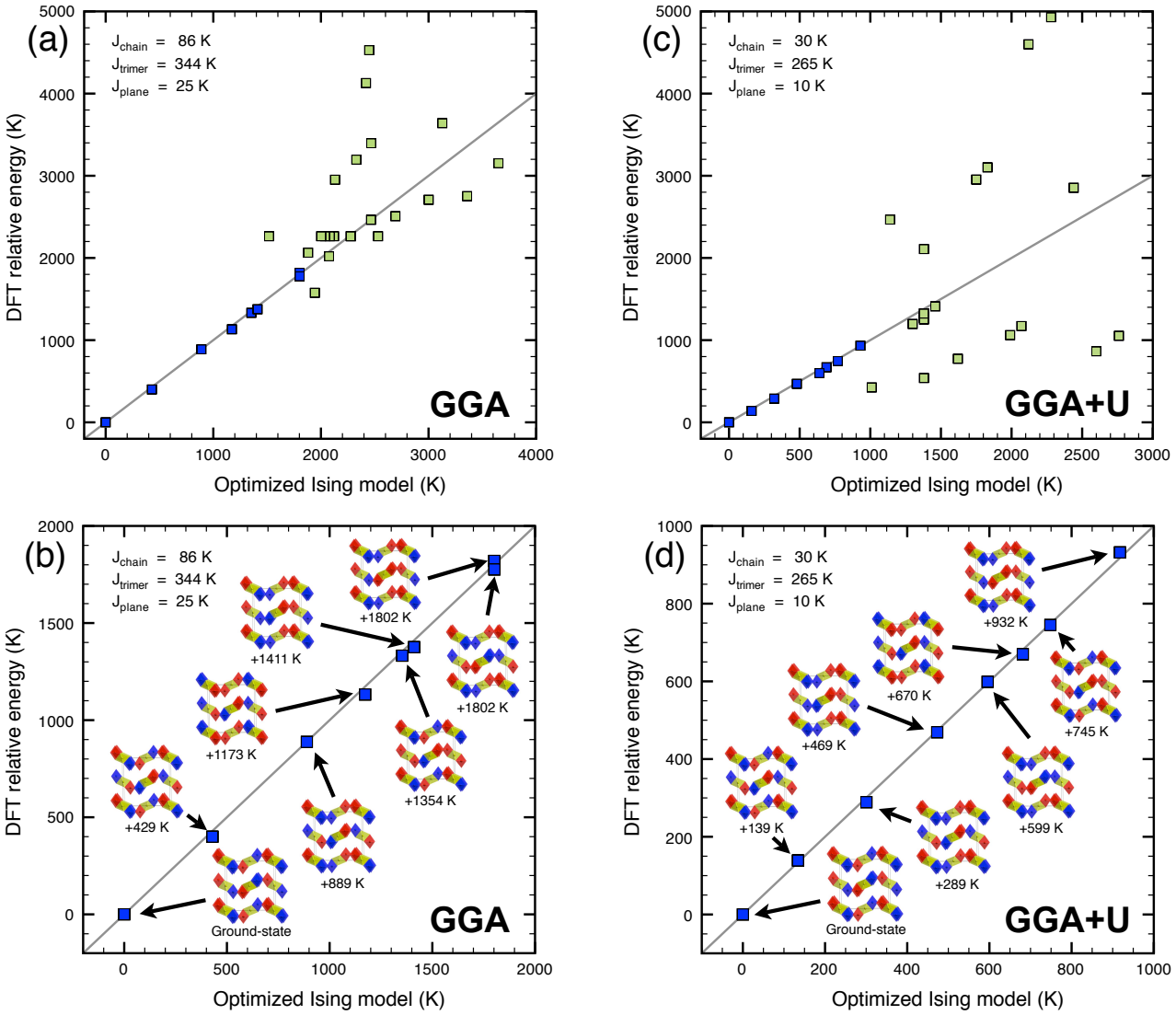

FIG. 4: (color online) (a) Results of the least-square fitting procedure employed to calculate magnetic couplings in GGA: only the low-energy configurations shown in blue have been used, the configurations shown in green have been discarded. The energy of the ground-state AFM configuration is used as the reference energy. (b) Detailed presentation of the 8 low-energy configurations considered for the evaluation of magnetic couplings. (c) and (d) show the results of the same procedure applied to GGA+U. Red (blue) $Ru(2)O_6$ coordination octahedra correspond to up (down) arrangements of the Ru(2) magnetic moments. According to the convention used in Eq. (1), AFM couplings are positive.

of the Ru(2) moments within the trimers and between adjacent trimers of the same layer, i.e. on the zig-zag chains running along a. The staking of these AFM layers along b is ferromagnetic (FM). It should be added that in this ground-state AFM structure, Ru(1) ions are non-magnetic in both GGA and GGA+U. A summary of the magnetic moments calculated in the muffin-tin spheres for both a FM and the ground state AFM spin arrangements is presented in Tab. I. These results are in perfect agreement with the magnetic structure deduced from neutron diffraction, which indicates that Ru(1) moments are not ordered whereas Ru(2) moments order with a propagation vector $\mathbf{k} = (0, 0, 0)$. The eight Ru(2) ions on the $8f$ site exhibit magnetic moments whose signs follow the $(+, +, -, -, +, +, -, -)$ sequence[12].

Total DOS and $4d$-LDOS of Ru(1) and one of the two Ru(2) of the trimer calculated in GGA+U for this ground-state configuration are shown in Fig. 3(a), (b) and (c) respectively. By symmetry, the magnetic moment of Ru(1) cancels through a double occupation of both t_{2g}^{+} and t_{2g}^{-} orbitals. Ru(2) ions, on the contrary, are strongly spin-polarized and adopt an electronic configuration close to the ionic low-spin $S = 1$ configuration with a single occupation of both t_{2g}^{+} and t_{2g}^{-} orbitals and a

TABLE II: Magnetic couplings between Ru(2) ions treated as $S = 1$ spins and extracted from the optimization of Eq. (2) for the 8 low-energy configurations shown in Fig. 4(b) and (d). According to the convention used in Eq. (2), AFM couplings are positive.

	J_{trimer} (K)	J_{chain} (K)	J_{plane} (K)
GGA	344	86	25
GGA+U	265	30	10

weaker polarization of the t_{2g}^0 states. The resulting magnetic moment on Ru(2) is 1.22 μ_B, largely reduced by covalent interactions from the expected value for a low-spin configuration (2 μ_B). It should be added here that the polarization of Ru(1) ions depends on the spin configuration under study but never exceeds 0.11 μ_B in GGA+U. The next important step of this work consists in the evaluation of the couplings occurring in $Ba_4Ru_3O_{10}$ between magnetic Ru(2) ions. In the broken symmetry formalism, the evaluation of these couplings is based on the mapping of total energies corresponding to various spin arrangements within a supercell onto an Heisenberg Hamiltonian

$$\hat{H} = \hat{H}_0 + \sum_{i>j} J_{ij} \hat{\mathbf{S}}_\mathbf{i} \hat{\mathbf{S}}_\mathbf{j} \qquad (1)$$

where $\hat{H}_0$ is the spin-independent part of the Hamiltonian, J_{ij} are the magnetic couplings to determine and $\hat{\mathbf{S}}_\mathbf{i}$ and $\hat{\mathbf{S}}_\mathbf{j}$ are, in our case, the $S = 1$ spin operators localized on Ru(2) sites i and j respectively. It is straightforward to show that the expectation value of Hamiltonian (1) on a DFT state $|\alpha\rangle$ (obtained by preparing the initial electron density according to a particular collinear spin arrangement in the supercell and performing a self-consistent calculation until convergence) can be simply written under the form of an Ising Hamiltonian[19]

$$\epsilon_\alpha^{DFT} = \langle\alpha|\hat{H}|\alpha\rangle = \epsilon_0 + S^2 \sum_{i>j} J_{ij}\sigma_i\sigma_j \qquad (2)$$

with $\sigma_i = \pm 1$ and here, $S = 1$. In strongly localized systems, such as $3d$ transition metal oxides, Eq. (2) can be employed to model large sets of spin configurations and a least-square minimization of the difference between DFT and Ising relative energies, can be applied to obtain a numerical evaluation of the couplings[20,21].

In our present case however, this procedure fails to fit accurately the energies of the 30 spin configurations, i.e. no single set of magnetic couplings can be used in Eq. (2) to describe correctly their relative energies. This procedure is however well adapted to describe a subset of low-energy configurations found right above the ground-state AFM order. In both cases, the same subset of 8 configurations (shown in blue in Fig. 4) including the AFM ground-state has been used. Three magnetic couplings, shown in Fig. 1, have been employed to obtain these results : the intra-trimer coupling J_{trimer} (5.10 Å), the inter-trimer coupling J_{chain} (3.92 Å) occurring between trimers of the same corrugated planes, i.e. between Ru(2) ions forming the zig-zag chains running along a and finally J_{plane}(5.87 Å) between nearest-neighbour Ru(2) ions of adjacent planes. It should be noted here that the use of these 30 spin configurations allows for the calculation of additional couplings between the planes but that their inclusion in the fitting procedure leads to negligible values and does not modify the values of the dominant couplings nor improves the quality of the fit.

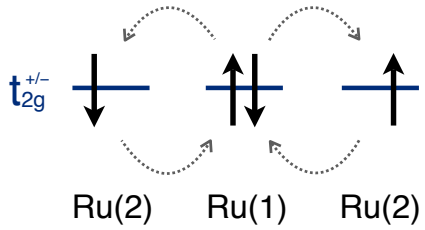

FIG. 5: (color online) Schematic of the kinetic superexchange mechanism proposed to explain the AFM coupling within the trimers.

The resulting magnetic couplings are summarized in Tab. II. Several conclusions can be drawn from these results. Firstly, both approximations lead to a consistent overall picture of the magnetic interactions in this compound where a dominant AFM interaction occurs within the structural trimers (J_{trimer}) coupled by weaker AFM interactions either in the corrugated planes (J_{chain}) or between these planes (J_{plane}). As shown in Fig. 5, the dominant AFM coupling J_{trimer} can be understood by the particular occupation scheme of the t_{2g}^+ and t_{2g}^- orbitals in the Ru(2)-Ru(1)-Ru(2) trimer supporting the hypothesis of an AFM interaction between moments localized on the Ru(2) ions through a kinetic superexchange[23] mechanism mediated by the Ru(1) orbitals or, more precisely, by Ru(1)-O hybrids.

Secondly, inclusion of the Hubbard U term in the calculations, employed here to improve the description of electron correlation occurring within the Ru-$4d$ states, leads to a reduction of the amplitude of these AFM couplings. This effect, also observed in other Ru-based systems[22], is consistent with the expected U-dependence of the AFM contribution to the magnetic couplings derived from the one-band Hubbard model $J^{AFM} \approx 4t^2/U$ where t and U are respectively the hopping and on-site Coulomb repulsion parameters.

Thirdly, as mentioned above and as it can be clearly seen in Fig. 4(a) and (c), large discrepancies are found between DFT and Ising relative energies for most of the high-lying spin configurations. To explain this behaviour, one has to consider that the spin Hamiltonian described by Eq. (1) relies on the assumption that the spatial part of the electronic wavefunctions does not depend on the particular spin arrangement employed in the supercell. If

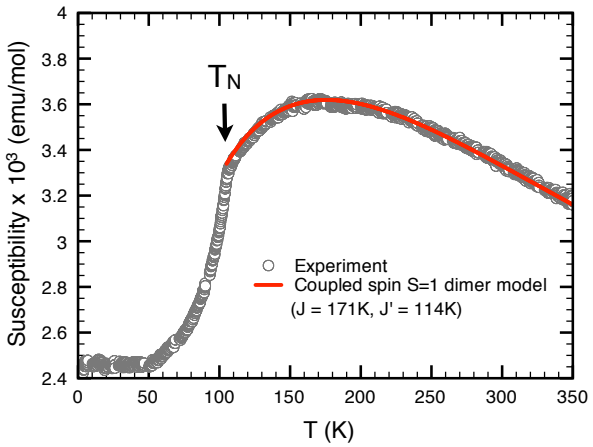

FIG. 6: (color online) Magnetic susceptibility of $Ba_4Ru_3O_{10}$ recorded up to 350 K fitted using Eq.(3).

this assumption is relatively well verified in strongly localized $3d$ systems, it is certainly much more questionable in the case of more extended Ru-$4d$ orbitals and in particular in $Ba_4Ru_3O_{10}$ where strong covalent metal-metal bonding occurs. One might therefore expect that only a (low-energy) part of the wide range of magnetic excitations covered by our set of spin configurations verifies approximately this assumption.

C. Magnetic susceptibility

These results led us to reinterpret the magnetic susceptibility of this compound above T_N as that of an ensemble of coupled $S = 1$ spin AFM dimers, i.e. to consider a structural trimer as a magnetic dimer where $S = 1$ spins are hold by the Ru(2) ions and where the Ru(1) is non-magnetic. Modelling the magnetic excitations of independent $S = 1$ spin dimers with an Heisenberg Hamiltonian characterized by the intra-dimer coupling $J_{\rm trimer}$, one can easily derive the expression of the molar magnetic susceptibility for this system as

$$\chi_{\rm dim} = \frac{2\beta g^2 \mu_B^2 N_A [1 + 5\exp(-2\beta J_{\rm trimer})]}{[3 + \exp(\beta J_{\rm trimer}) + 5\exp(-2\beta J_{\rm trimer})]} \qquad (3)$$

where $\beta = 1/k_B T$, N_A is the Avogadro number, μ_B is the Bohr magneton and $g = 2$. Treating the inter-dimer interactions through a mean-field approximation, one further obtains[24,25]

$$\chi = \frac{\chi_{\rm dim}}{(1 + \lambda \chi_{\rm dim})} + \chi_0 \qquad (4)$$

where $\lambda = J_{\rm inter}/N_A(g\mu_B)^2$, $J_{\rm inter} \approx 2J_{\rm chain} + 2J_{\rm plane}$, χ_0 is a temperature-independent contribution and $\chi_{\rm dim}$ is the susceptibility of $S = 1$ dimers as defined in Eq. (3).

Magnetic susceptibility has been measured within a Physical Property Measurement System (PPMS) from Quantum Design equipped with a vibrating sample magnetometer. Data have been collected under a magnetic field of 0.1 T in the field-cooled mode. The fit of this experimental magnetic susceptibility for the 110-350 K range is shown in Fig. 6. This fit was obtained for $J_{\rm trimer} = 171$ K, $J_{\rm inter} = 114$ K and $\chi_0 = 2.10^{-4}$ emu/mol. Both intra- and inter-trimer couplings are AFM with a dominant intra-trimer coupling. The picture drawn from this analysis is therefore compatible with the one deduced from DFT of $S = 1$ spins hold by the Ru(2) ions only coupled by a strong AFM interaction within the structural trimers and interacting with each other through weaker AFM inter-trimer couplings. It should be mentioned here that this fit is also compatible with the intermediate- and high-temperature measurements from T_N up to ~ 612 K performed by Dussarrat *et al.*[26].

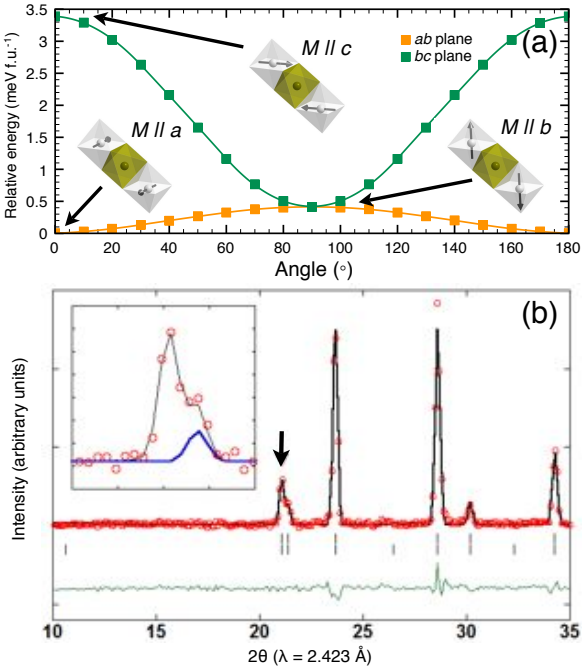

FIG. 7: (color online) (a) Dependence of energy on the direction of the Ru(2) magnetic moments in the ab and bc planes calculated for the ground-state AFM order in GGA+U+SO. (b) Rietveld refinement of the neutron powder diffraction pattern recorded at 1.8 K[12]. Red circles, black and green lines represent the observed, calculated and difference patterns, respectively. The expected positions of the Bragg reflections are shown as vertical bars: the upper series correspond to the nuclear phase, while the lower series marks the magnetic contribution. The inset shows an enlargement of the (020)/(002) doublet (marked by an arrow), with the blue line corresponding to magnetic contribution to the total intensity.

D. Magnetocrystalline anisotropy

To complete our analysis and lift the ambiguity on the orientation of the magnetic moments left by neutron diffraction measurements[12], GGA+U+SO calculations have been carried out for the ground-state AFM order within the framework of *collinear* magnetism. This approximation is mainly justified by the fact that only the (002) Bragg reflection presents an extra magnetic contribution below T_N in neutron diffraction[12], limiting considerably the data available to refine potential non-collinear structures. The DFT total energy dependence upon the Ru(2) magnetization orientation has been systematically calculated in the *ab* and *bc* planes, as shown in Fig. 7(a). These results clearly point out *a* as the magnetization direction minimizing the total energy. These results can be understood qualitatively by considering the crystal-field levels of Ru(2) shown in Fig. 3(c) and treating the SO as a local perturbation. The SO Hamiltonian $\hat{H}_{\rm so} = \xi\ \hat{\mathbf{L}}\cdot\hat{\mathbf{S}}$ can be written, for an orientation of the magnetization along $\mathbf{n}(\theta,\phi)$ (θ and ϕ are respectively the polar and azimuthal angles in the local coordinate system shown in Fig. 1(b)), as follows[27] :

$$\begin{aligned}\hat{H}_{\rm so} = \xi\ \hat{S}_n &\left(\hat{L}_z\cos\theta + \frac{1}{2}\hat{L}_+e^{-i\phi}\sin\theta + \frac{1}{2}\hat{L}_-e^{i\phi}\sin\theta\right)\\ +\frac{1}{2}\hat{S}_+ &\left(-\hat{L}_z\sin\theta - \hat{L}_+e^{-i\phi}\sin^2\frac{\theta}{2} + \hat{L}_-e^{i\phi}\cos^2\frac{\theta}{2}\right)\\ +\frac{1}{2}\hat{S}_- &\left(-\hat{L}_z\sin\theta + \hat{L}_+e^{-i\phi}\cos^2\frac{\theta}{2} - \hat{L}_-e^{i\phi}\sin^2\frac{\theta}{2}\right)\end{aligned}$$

Assuming, as it could be expected from Fig. 3(c), that leading terms in the second-order non-degenerate perturbation expansion imply $\langle t_{2g}^{+\uparrow}|\hat{H}_{\rm so}|t_{2g}^{-\downarrow}\rangle$ and $\langle t_{2g}^{-\uparrow}|\hat{H}_{\rm so}|t_{2g}^{+\downarrow}\rangle$ matrix elements, both proportional to $-(i\xi\sin\theta)/2$, the SO stabilization is maximized for $\theta = \pi/2$ and thus fixes the magnetization in the plane perpendicular to the local z axis, i.e. perpendicular to the Ru-Ru bond. The sole magnetization direction able to satisfy this condition in $Ba_4Ru_3O_{10}$ within the approximation of collinear magnetism is therefore *a*. This result is consistent with the neutron powder diffraction as shown in Fig. 7(b) through the Rietveld refinement of the magnetic structure using the AFM ground-state order with a magnetization laying along *a* and a magnetic moment of 1.11(11) μ_B on the Ru(2) ions only (to be compared to 1.22 μ_B from GGA+U calculations, see Tab. I).

IV. SUMMARY

In conclusion, this work emphasizes the dominant role played by Ru-Ru covalent interactions on the magnetism of $Ba_4Ru_3O_{10}$ along with crystal-field effects, electron correlation and spin-orbit coupling. In particular, it provides a new picture of this compound where structural trimers behave as magnetic dimers of $S = 1$ spins hold by the Ru(2) ions in the low-spin electronic configuration, the Ru(1) ions being essentially non-magnetic. The phase transition observed at T_N might therefore be considered as a transition from a state dominated by short-range intra-trimer AFM interactions to a Néel order mediated by weaker inter-trimer AFM interactions.

Acknowledgements

Y.K. thanks the staff of the *Low Temperature Physics* plateforme (UPMC).

* Electronic address: guillaume.radtke@impmc.upmc.fr

[1] R. J. Cava, Dalton Trans., 2979 (2004).
[2] P. Khalifah, R. Osborn, Q. Huang, H.W. Zandbergen, R. Jin, Y. Liu, D. Mandrus and R.J. Cava, Science 297, 2237 (2002).
[3] V. Eyert, S.G. Ebbinghaus and T. Kopp, Phys. Rev. Lett. 96, 256401 (2006).
[4] H. Wu, Z. Hu, T. Burnus, J.D. Denlinger, P.G. Khalifah, D.G. Mandrus, L.-Y. Jang, H.H. Hsieh, A. Tanaka, K.S. Liang, J.W. Allen, R.J. Cava, D.I. Khomskii and L.H. Tjeng, Phys. Rev. Lett. 96, 256402 (2006).
[5] S.J. Moon, W.S. Choi, S.J. Kim, Y.S. Lee, P.G. Khalifah, D. Mandrus and T.W. Noh, Phys. Rev. Lett. 100, 116404 (2008).
[6] D. Wu, P.G. Khalifah, D.G. Mandrus and N.L. Wang, J. Phys.: Condens. Matter 20, 325204 (2008).
[7] S. Lee, J.-G. Park, D.T. Adroja, D. Khomskii, S. Streltsov, K. A. McEwen, H. Sakai, K. Yoshimura, V.I. Anisimov, D. Mori, R. Kanno and R. Ibberson, Nature Materials 5, 471 (2006).
[8] J.P. Carlo, T. Goko, I.M. Gat-Malureanu, P.L. Russo, A.T. Savici, A.A. Aczel, G.J. MacDougall, J.A. Rodriguez, T.J. Williams, G.M. Luke, C.R. Wiebe, Y. Yoshida, S. Nakatsuji, Y. Maeno, T. Taniguchi and Y.J. Uemura, Nature Materials 11, 323 (2012).
[9] Y. Maeno, H. Hashimoto, K. Yoshida, S. Nishizaki, T. Fujita, J.G. Bednorz and F. Lichtenberg, Nature 372, 532 (1994).
[10] V.I. Anisimov, I.A. Nekrasov, D.E. Kondakov, T.M. Rice and M. Sigrist, Eur. Phys. J. B 25, 191 (2002).
[11] D. Fobes, E. Vehstedt, J. Peng, G.C. Wang, T.J. Liu and Z.Q. Mao, J. Appl. Phys. 111, 083709 (2012).
[12] Y. Klein, G. Rousse, F. Damay, F. Porcher, G. André, and I. Terasaki, Phys. Rev. B **84**, 054439 (2011).
[13] P. Blaha, K. Schwarz, G. Madsen, D. Kvaniscka, and J. Luitz, in Wien2k, An Augmented Plane Wave Plus Local Orbitals Program for Calculating Crystal Properties, edited by K. Schwarz Vienna University of Technology, Vienna, Austria, 2001.
[14] J.P. Perdew, K. Burke and M. Ernzerhof, Phys. Rev. Lett.

77, 3865 (1996).
[15] V.I. Anisimov, I.V. Solovyev, M. A. Korotin, M. T. Czyżyk and G.A. Sawatzky, Phys. Rev. B **48**, 16929 (1993).
[16] J. Kuneš, P. Novák, M. Diviš, P.M. Oppeneer, Phys. Rev. B **63**, 205111 (2001) and references therein.
[17] S.V. Streltsov and D.I. Khomskii, Phys. Rev. B **86**, 064429 (2012).
[18] C. J. Ballhausen, *Introduction to ligand field theory* McGraw-Hill Book Compagny, New York, San Francisco, Toronto, London (1962).
[19] G. Radtke, A. Saúl, H.A. Dabkowska, G.M. Luke and G.A. Botton, Phys. Rev. Lett. **105**, 036401 (2010).
[20] A. Saúl and G. Radtke, Phys. Rev. Lett. **106**, 177203 (2011).
[21] A. Saúl D. Vodenicarevic and G. Radtke, Phys. Rev. B **87**, 024403 (2013).
[22] F. Wu, E. Kan, M.-H. Whangbo, Inorg. CHem. **49**, 3025 (2010).
[23] G.A. Sawatzky, W. Geertsma and C. Haas, J. Magn. Magn. Mat. **3**, 37 (1976).
[24] W. Miiller, M. Avdeev, Q. Zhou, A.J. Studer, B.J. Kenndy, G.J. Kearley and C.D. Ling, Phys. Rev. B **84**, 220406(R) (2011).
[25] M. Uchida, H. Tanaka, M.I. Bartashevich and T. Goto, J. Phys. Soc. Jap. **70**, 1790 (2001).
[26] C. Dussarrat, F. Grasser, R. Bontchev and J. Darriet, J. All. Comp. **233**, 15 (1996).
[27] X. Wang, R. Wu, D.-S. Wang, A.J. Freeman, Phys. Rev. B **54**, 61 (1996).